ELECTROCHEMISTRY

A universal wet-chemistry synthesis of solid-state halide electrolytes for all-solid-state lithium-metal batteries

Changhong Wang[1†], Jianwen Liang[1†], Jing Luo[1], Jue Liu[2], Xiaona Li[1], Feipeng Zhao[1], Ruying Li[1], Huan Huang[3], Shangqian Zhao[4], Li Zhang[4], Jiantao Wang[4]*, Xueliang Sun[1]*

Solid-state halide electrolytes have gained revived research interests owing to their high ionic conductivity and high-voltage stability. However, synthesizing halide electrolytes from a liquid phase is extremely challenging because of the vulnerability of metal halides to hydrolysis. In this work, ammonium-assisted wet chemistry is reported to synthesize various solid-state halide electrolytes with an exceptional ionic conductivity (>1 microsiemens per centimeter). Microstrain-induced localized microstructure change is found to be beneficial to lithium ion transport in halide electrolytes. Furthermore, the interfacial incompatibility between halide electrolytes and lithium metal is alleviated by transforming the mixed electronic/ionic conductive interface into a lithium ion–conductive interface. Such all-solid-state lithium-metal batteries (ASSLMBs) demonstrate a high initial coulombic efficiency of 98.1% based on lithium cobalt oxide and a high discharge capacity of 166.9 microampere hours per gram based on single-crystal $LiNi_{0.6}Mn_{0.2}Co_{0.2}O_2$. This work provides universal approaches in both material synthesis and interface design for developing halide-based ASSLMBs.

INTRODUCTION

All-solid-state lithium-metal batteries (ASSLMBs) are attracting tremendous attention because of their high theoretical energy density and much-improved safety (*1*, *2*). To develop ASSLMBs, a solid-state electrolyte is an indispensable component to replace conventional organic separators and flammable organic liquid electrolytes. Meanwhile, lithium metal anodes are used to boost the energy density (*3*, *4*). Over the past decades, various solid-state electrolytes have been developed, such as polymer electrolytes (*5*–*7*), oxide electrolytes (*8*, *9*), sulfide electrolytes (*10*), borohydrides (*11*–*15*), and recently revived halide electrolytes (Li_3MX_6, M = Y and In; X = Cl, Br, and I) (*16*, *17*). Among them, polymer electrolytes show excellent flexibility and viability for manufacturing but low room temperature (RT) ionic conductivity (*5*–*7*). Oxide electrolytes demonstrated high ionic conductivity and wide electrochemical windows but unfavorable mechanical stiffness for processing (*8*, *9*). Sulfide electrolytes exhibit high ionic conductivity and soft mechanical properties but poor air stability, being prone to release toxic H_2S gas upon exposure to humid air (*18*). Recently, solid-state halide electrolytes (e.g., Li_3YCl_6 and Li_3YBr_6) have gained substantial research attention because of their high ionic conductivity (>1 mS cm^{-1}), high-voltage cathode compatibility, and favorable mechanical properties for directly cold sintering for intimate solid-solid ionic contact (*19*). Compared to sulfide electrolytes, solid-state halide electrolytes do not release harmful H_2S gas when exposed to the ambient environment and have better high-voltage stability and wider electrochemical windows, making them attractive and feasible for ASSLMBs toward high safety and high energy density (*16*).

Inspired by these advantages, research into halide electrolytes has rapidly revived in recent years. For example, our group developed Li_3InCl_6 (*20*–*23*), Li_3ScCl_6 (*24*), and $Li_3Y_{1-x}In_xCl_6$ (*25*); optimized Li_3YBr_6 (*26*); and provided comprehensive reviews about halide electrolytes (*16*, *17*). Nazar and coworkers also synthesized $Li_{3-x}M_{1-x}Zr_xCl_6$ (M = Y and Er) (*27*) and spinel $Li_2Sc_{2/3}Cl_4$ (*28*) with a disordered spinel structure. Zeier and coworkers investigated Li_3YCl_6 (*29*), Li_3ErCl_6 (*29*, *30*), $Na_{3-x}Er_{1-x}Zr_xCl_6$ (*31*), and Li_3ErI_6 (*32*). Jung and coworkers (*33*) developed cost-effective Fe-doped Li_2ZrCl_6. Besides, β-Li_3AlF_6 has also been synthesized with a low RT ionic conductivity (*34*), which could be useful as a surface coating material for the high-voltage cathodes (*35*). Along with the experimental progress, theoretical calculations were widely used to predict the electrochemical stability and ionic conductivity of halide electrolytes (*30*, *36*–*39*). Most of these halide electrolytes were synthesized by a mechanochemical approach. So far, only Li_3InCl_6 can be synthesized from an aqueous solution for easy scale-up, as demonstrated in our previous work with a hydrate intermediate ($Li_3InCl_6 \cdot nH_2O$) (*20*). Other halide electrolytes cannot be synthesized from the solvent-assisted process because of the easy hydrolysis of $MCl_3 \cdot nH_2O$ upon heating. Considering the wet-chemistry method with great advantages in controlling the morphology and size of solid electrolytes as well as fabricating sheet-typed electrodes with intimate solid-solid ionic contact for practical pouch cell manufacturing (*22*, *40*), it is of great importance to develop a general wet-chemistry route to synthesize halide electrolytes with a decent ionic conductivity.

On the other hand, using lithium metal as the anode to realize ASSLMBs is compulsory to realize the high energy density competitive with that of the prevailing lithium-ion batteries based on liquid electrolytes (*3*). However, the poor interfacial stability between halide electrolytes and lithium metal is another concern for the successful application of halide electrolytes in ASSLMBs (*41*). Therefore, a rational design of the anode interface between halide electrolytes and lithium metal is an urgent task for propelling ASSLMBs.

With the two motivations in mind, we report ammonium-assisted wet chemistry to synthesize solid-state halide electrolytes. Inspired

---

[1]Department of Mechanical and Materials Engineering, University of Western Ontario, 1151 Richmond St., London, Ontario N6A 3K7, Canada. [2]Neutron Scattering Division, Oak Ridge National Laboratory, Oak Ridge, TN 37831, USA. [3]Glabat Solid-State Battery Inc., 700 Collip Circle, London, Ontario N6G 4X8, Canada. [4]China Automotive Battery Research Institute Co. Ltd., 5th Floor, No. 43, Mining Building, North Sanhuan Middle Road, Haidian District, Beijing P.C. 100088, China.
*Corresponding author. Email: wangjt@glabat.com (J.W.); xsun9@uwo.ca (X.S.)
†These authors contributed equally to this work.

by the industrial "ammonium chloride route" to synthesize anhydrous MCl_3 (M = trivalent metals) (*42*, *43*), the most common issue of the MCl_3 hydrolysis in water is inhibited by the formation of $(NH_4)_3[MCl_6]$ intermediates. Therefore, the ammonium-assisted wet-chemistry synthesis is developed to be a universal approach to obtaining various solid-state halide electrolytes. Taking Li_3YCl_6 as an example, Li_3YCl_6 with an RT ionic conductivity of 0.345 mS cm^{-1} was successfully achieved. To demonstrate the universality, Li_3ScCl_6, Li_3YBr_6, and Li_3ErCl_6 were obtained with high ionic conductivity of 1.25, 1.09, and 0.407 mS cm^{-1}, respectively. Localized microstrain–induced microstructural change is found to be beneficial for Li^+ transport along the *ab* plane, thus improving the ionic conductivity. Moreover, the long-standing anode interface issue between halide electrolytes and lithium metal was resolved by changing the mixed Li^+/e^--conductive interface into a Li^+-conductive interface, effectively preventing the continuous reduction and degradation of halide electrolytes. As a result, halide-based ASSLMBs are successfully constructed with excellent electrochemical performance. It should be mentioned that this is the first time to report halide-based ASSLMBs with exceptional electrochemical performance, eliminating the considerable concern for their anode interface incompatibility. The present study lays the groundwork for future research into halide-based ASSLMBs toward high energy density and excellent safety.

RESULTS

Ammonium-assisted wet-chemistry synthesis of solid-state halide electrolytes

We first tried to synthesize Li_3YCl_6 via a wet-chemistry approach with various solvents, such as ethanol, tetrahydrofuran, and acetonitrile, as these solvents can dissolve YCl_3 and LiCl. However, only impurities LiCl and yttrium oxychloride (YOCl) were observed by x-ray diffraction (XRD) patterns (fig. S1). Inspired by the traditional "ammonium halide routes" to produce highly pure MCl_3, in which NH_4Cl is used as the coordination reagent, we purposely added NH_4Cl into the solvents to coordinate with YCl_3 forming $(NH_4)_3[YCl_6]$ intermediate (*42*, *43*). During the following thermal decomposition process, LiCl reacts with $(NH_4)_3[YCl_6]$ to produce Li_3YCl_6. Below is the proposed reaction route (*42*)

$$MCl_3 \cdot nH_2O + 3NH_4Cl \xrightarrow{H_2O} (NH_4)_3[MCl_6]$$

$$(NH_4)_3[MCl_6] + 3LiCl \xrightarrow{\text{Heating}} Li_3MCl_6 + 3NH_3 + 3HCl$$

M^{3+} represents the trivalent Y^{3+}, Sc^{3+}, Er^{3+}, etc. The solvent is deionized water, which is cheap, abundant, and environmentally friendly. The $(NH_4)_3[YCl_6]$ intermediate was identified by XRD (fig. S2). The intermediate $(NH_4)_3[YCl_6]\cdot 3LiCl$ composite can be completely decomposed at around 400°C, as analyzed by thermogravimetry analysis and differential scanning calorimetry (TGA-DSC) (Fig. 1A). The large endothermic peaks lower than 400°C are related to ammonium decomposition, while the small endothermic peaks above 400°C indicate the formation of the Li_3YCl_6 phase. On the basis of the TGA-DSC results, the complex chlorides were annealed at 350°, 400°, 450°, 500°, and 550°C for 5 hours under Ar atmosphere. As synthesized Li_3YCl_6 from different temperatures are named as Li_3YCl_6-350, Li_3YCl_6-450, Li_3YCl_6-500, and Li_3YCl_6-550, respectively. The XRD patterns of these Li_3YCl_6 samples are displayed in Fig. 1B. After heating at 350°C, the obtained powder contained a lot of LiCl precursor and barely any Li_3YCl_6, suggesting that 350°C was not enough to fully decompose the intermediate $(NH_4)_3[YCl_6]$ or form Li_3YCl_6 phase. Heating above 400°C, both LiCl and Li_3YCl_6 were observed by XRD, suggesting that LiCl partially reacted with $(NH_4)_3[YCl_6]$. Further increasing the heating temperature to above 450°C, mainly XRD characteristics of Li_3YCl_6 were shown with the suppressed characteristic peak of LiCl at 34.55° (highlighted by a green bar). Heat treatment at higher temperatures can increase the crystallinity of Li_3YCl_6 and decrease the LiCl impurity, as suggested by the XRD results of Li_3YCl_6-500 and Li_3YCl_6-550. However, high-crystallinity may not be beneficial for its ionic conductivity, as suggested in previous studies (*19*). Figure 1C displays the slow-scanned XRD pattern and Rietveld refinement result of Li_3YCl_6-500. Li_3YCl_6 consists of a hexagonal close-packed anion arrangement with trigonal *P*-3*m*1 space group (ICSD no. 04-009-8882); all the cations are sited at the octahedral center. Table S1 shows the detailed structural information of the Rietveld refinement results, which are compared with the structure information of Li_3YCl_6 in the database. The XRD refinement result also showed that the content of LiCl impurity was about 4.3 weight % (wt %).

The particle size of the as-synthesized Li_3YCl_6-500 is around 400 nm, while the crystallize size is only 159.11 nm (Fig. 1D and fig. S3), which is significantly smaller than the micrometer size of Li_3YCl_6 synthesized by the mechanochemical method or comelting method (*44*). It is well known that the small size effect would induce localized microstrain in materials because of the localized disturbance in the lattice or defect formation. To understand the microstrain effect on the ionic conductivity of as-prepared halide electrolytes, we quantified the microstrain in small-size Li_3YCl_6 by the Williamson-Hall method. The microstrain in small Li_3YCl_6 was 0.118% (Fig. 1D). It was found that the bond lengths of Li4–Cl1, Li4–Cl3, and Li4–Cl3 were elongated as compared in fig. S4, which is the result of the microstrain (ε) induced by the local structure change. It is anticipated that the elongated Li—Cl bonds accelerate Li-ion transport along the *ab* plane (Fig. 1D), thereby increasing the ionic conductivity (table S3).

Fig. 2A shows the corresponding Arrhenius plots of Li_3YCl_6 obtained from different temperatures. The activation energy (E_a) is calculated by the Arrhenius Eq. 1

$$\sigma = \sigma_0 \exp(-E_a/k_B T)/T \tag{1}$$

where σ represents the ionic conductivity, σ_0 is a prefactor, *T* is the absolute temperature, and k_B is the Boltzmann constant. The RT ionic conductivities and corresponding activity energies of Li_3YCl_6 under various annealing temperatures are shown in Fig. 2B. The corresponding electrochemical impedance spectroscopy (EIS) profiles are shown in fig. S5.

The ionic conductivity of the Li_3YCl_6 increased with increasing annealing temperatures but decreases after 500°C. The highest RT ionic conductivity of 0.345 mS cm^{-1} is obtained at 500°C, with the lowest activation energy of 0.39 eV (Fig. 2B). The Li_3YCl_6 showed a higher ionic conductivity and lower activation energy than that synthesized by the comelting method (0.058 mS cm^{-1}; fig. S6) (*19*). The enhancement in the ionic conductivity is attributed to local structure distortion caused by the localized microstrain. The Li^+ transport

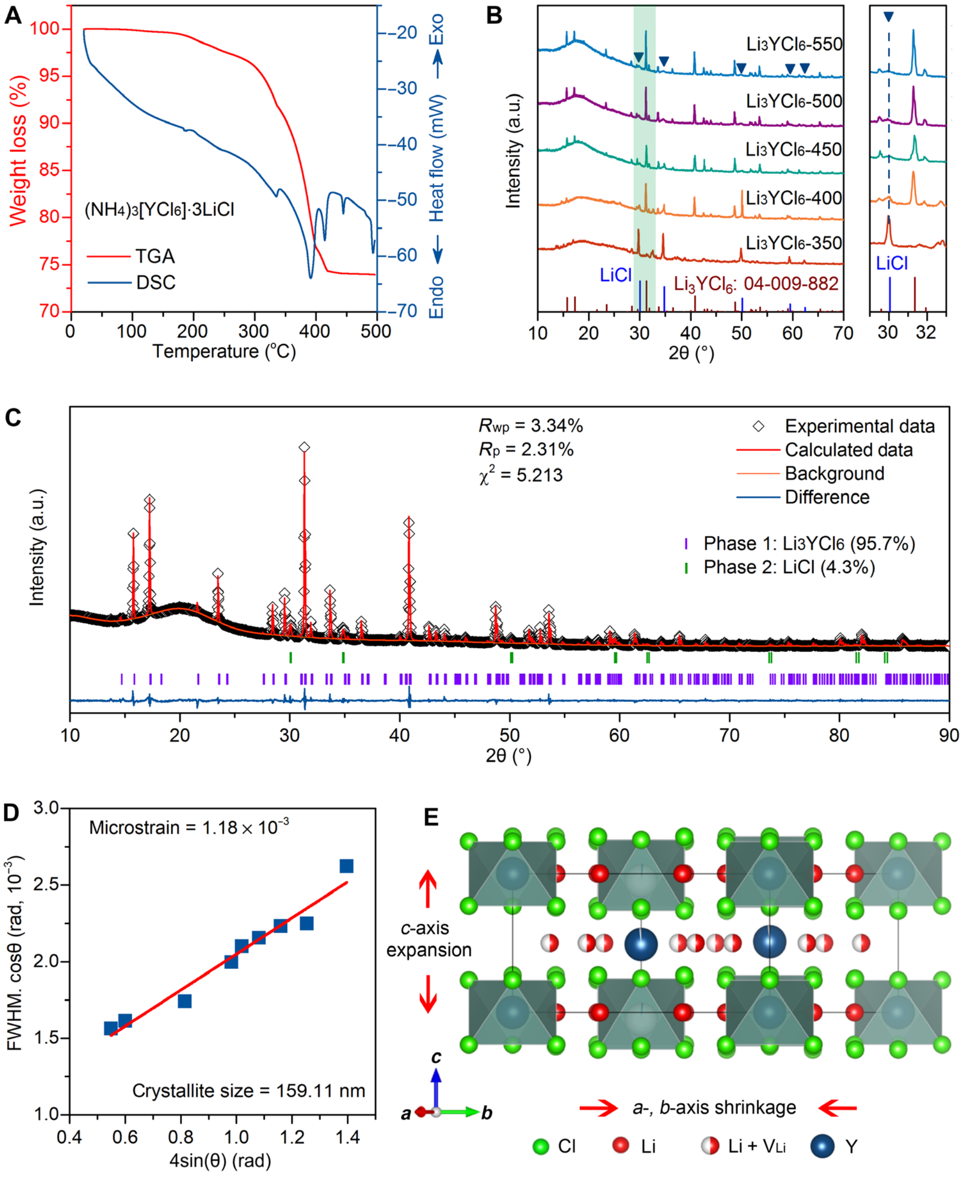

Fig. 1. Synthesis and structural analysis of wet-chemistry Li_3YCl_6. (**A**) TGA-DSC curves of $(NH_4)_3[YCl_6]\cdot 3LiCl$ composite. (**B**) XRD patterns of Li_3YCl_6 annealed under different temperatures. (**C**) Rietveld refinement of slow-scanned Li_3YCl_6-500. (**D**) Williamson-Hall plot. FWHM, full width at half maximum. (**E**) Crystal structure of wet-chemistry Li_3YCl_6 obtained from XRD refinement. a.u., arbitrary units.

kinetics was significantly enhanced in the *ab* plane, as confirmed by XRD refinement in Fig. 1 (C and D). A detailed discussion was made in the following section of the structure-to-property relationship. Figure 2C shows the evaluation of electronic conductivity of Li_3YCl_6 by direct current (DC) polarization analysis. The electronic conductivity of Li_3YCl_6 is 1.51×10^{-9} S.cm^{-1} (fig. S7). Note that the low electronic conductivity of Li_3YCl_6 is beneficial for lithium-dendrite suppression capability (*45*). Figure 2D demonstrated the stable electrochemical window of Li_3YCl_6 with 20% carbon as 0.65 to 4.25 V (versus Li^+/Li), which is close to the theoretical prediction (*37*). The wide electrochemical window of Li_3YCl_6 can tolerate the high-voltage cathodes beyond 4 V. At the anode side, Li_3YCl_6 is thermodynamically unstable against lithium metal because of the reduction of Y^{3+}; however, lithium metal can be used as long as a stable interface is built.

Universality demonstration and structure-to-performance relationship

As the ammonium-assisted route is a universal approach in industry to produce various anhydrous MX_3 (M = Tb-Lu, Y, and Sc; X = Cl, Br, and I) (*42*–*44*), the ammonium-assisted wet-chemistry approach can probably be a universal approach to synthesizing various halide electrolytes with a small size. To prove the generality, Li_3ScCl_6, Li_3ErCl_6, and Li_3YBr_6 were further synthesized by the wet-chemistry approach. Figure 3A shows the XRD pattern of Li_3ScCl_6. Different from the structure of Li_3YCl_6, Li_3ScCl_6 belongs to a monoclinic structure (*C*2/*m*, ICSD no. 04-009-8885) consisting of a cubic close-packed anion arrangement (*24*). All the cations site in the octahedral sites (fig. S8). Figure 3B exhibits the Arrhenius plot of Li_3ScCl_6, its RT ionic conductivity reached 1.25 mS cm^{-1}, and the corresponding activation

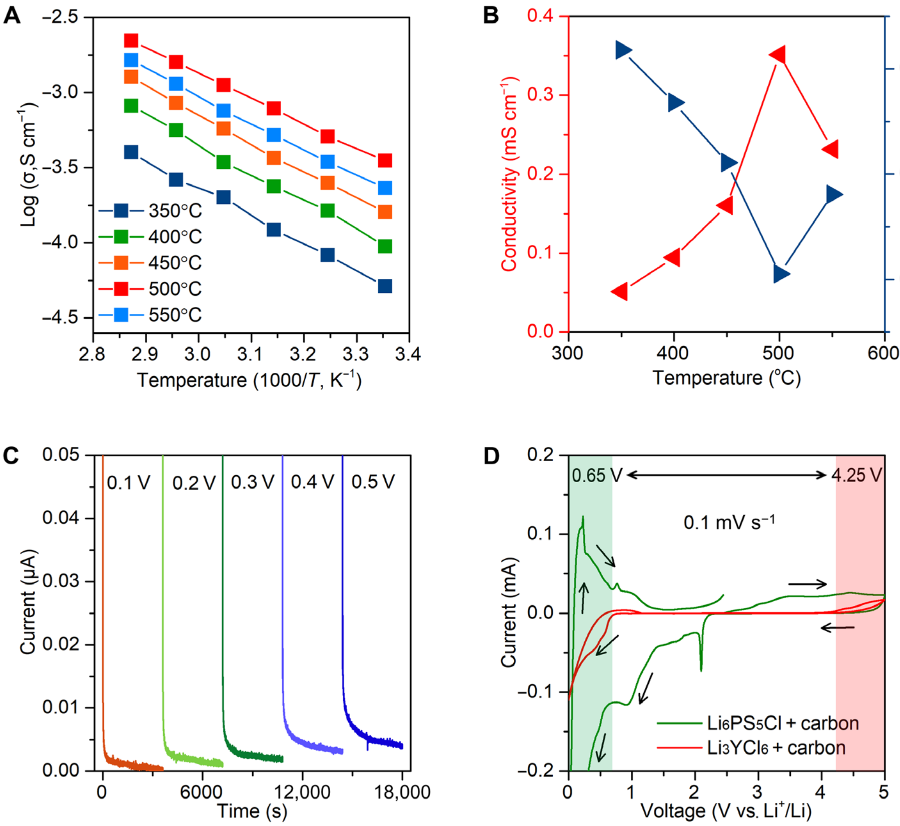

Fig. 2. Electrochemical properties of Li_3YCl_6 synthesized by the wet-chemistry method. (**A**) Arrhenius plot of wet-chemistry Li_3YCl_6 annealed under different temperatures. (**B**) The temperature-dependent RT ionic conductivities and activation energies. (**C**) DC polarization curves of wet-chemistry Li_3YCl_6 using symmetric cell configuration with different voltage biases from 0.1 to 0.5 V. (**D**) Cyclic voltammetry profile comparison between Li_6PS_5Cl and wet-chemistry Li_3YCl_6 (the working electrode side consists of 80 wt % electrolytes and 20 wt % carbon black).

energy is 0.31 eV. The high ionic conductivity was also confirmed by the electron-blocking DC test (fig. S9), suggesting that the main charge carriers are lithium ions. The electronic conductivity of Li_3ScCl_6 is only 1.38×10^{-9} S cm^{-1}. The scanning electron microscopy (SEM) image in Fig. 3C displays that the size of Li_3ScCl_6 is 200 to 500 nm. In parallel, Fig. 3D shows the refinement results of Li_3ErCl_6 synthesized by the wet-chemistry method. It also shows 3.7% LiCl impurity based on XRD refinement results. The RT ionic conductivity of Li_3ErCl_6 is 0.407 mS cm^{-1} with an activation energy of 0.47 eV, and the particle size is about 500 nm, as displayed in Fig. 3 (E and F). Not only the chloride-based halide electrolytes but also the bromide-based halide electrolytes can be synthesized. Figure S10A displays the refinement results of wet-chemistry Li_3YBr_6 with high purity, which have a high ionic conductivity of 1.08 mS cm^{-1} and a low activation energy of 0.34 eV (fig. S10, B and C). The successful synthesis of Li_3YCl_6, Li_3ScCl_6, Li_3ErCl_6, and Li_3YBr_6 proves that the ammonium-assisted wet-chemistry approach is a general approach to obtaining various halide electrolytes with a submicrometer size and decent ionic conductivity.

Furthermore, previous studies have proven that different synthesis methods have a strong influence on lattice distortion and atomic occupancy, which, in turn, affect ionic conductivity (*29*, *46*, *47*). However, the microstrain effect on the Li^+ transport properties has not been discussed yet. The microstrain induced by the small size confinement or defects has been reported to have a significant impact on the local structure of nanomaterials (*48*), thus affecting the Li^+ transport to some extent. To understand the microstrain effect on the Li^+ transport of solid-state halide electrolytes synthesized by the wet-chemistry method, the atomic occupation influence should be avoided. For this purpose, all XRD results of slow-scanned XRD profiles for wet-chemistry Li_3YCl_6, wet-chemistry Li_3ScCl_6, and wet-chemistry Li_3ErCl_6 were refined with the same occupation of cations (i.e., Y^{3+}, Sc^{3+}, Er^{3+}, and Li^+) in the same respective Wyckoff positions. By doing so, thus, the localized microstrain effect on the ionic conductivity can be fairly evaluated without the influence of cation disorder. First, crystal structures of wet-chemistry Li_3YCl_6 and wet-chemistry Li_3ScCl_6 were verified by time-of-flight neutron diffraction and were fully consistent with our previous results (fig. S11) (*17*, *24*). The atomic occupancies of Li_3ScCl_6 in table S4 are kept unchanged for slow-scanned XRD refinement results (table S5). The Sc—Cl bonds are expanded as compared in table S6; thus, Li^+ transport via [octa]-[tetra]-[octa] along the *c* axis is limited in comparison with the standard Li_3ScCl_6, which may be the underlying reason for the slightly lower ionic conductivity of Li_3ScCl_6 (Fig. 3B). The case of Li_3ErCl_6 is the same as the case of Li_3YCl_6, and the *c* axis is elongated, while the *a* axis and *b* axis are shrunk as compared in tables S7 and S8. The crystallite size of the Li_3ScCl_6 was determined to be 97.64 nm, and the microstrain is 0.166% (fig. S12), as calculated by the Williamson-Hall plot method. The microstrain in Li_3ErCl_6 was found to be 0.142%, and the crystallite size is 53.32 nm (fig. S12). In comparison, the wet-chemistry method may lead to microstrains that are several times

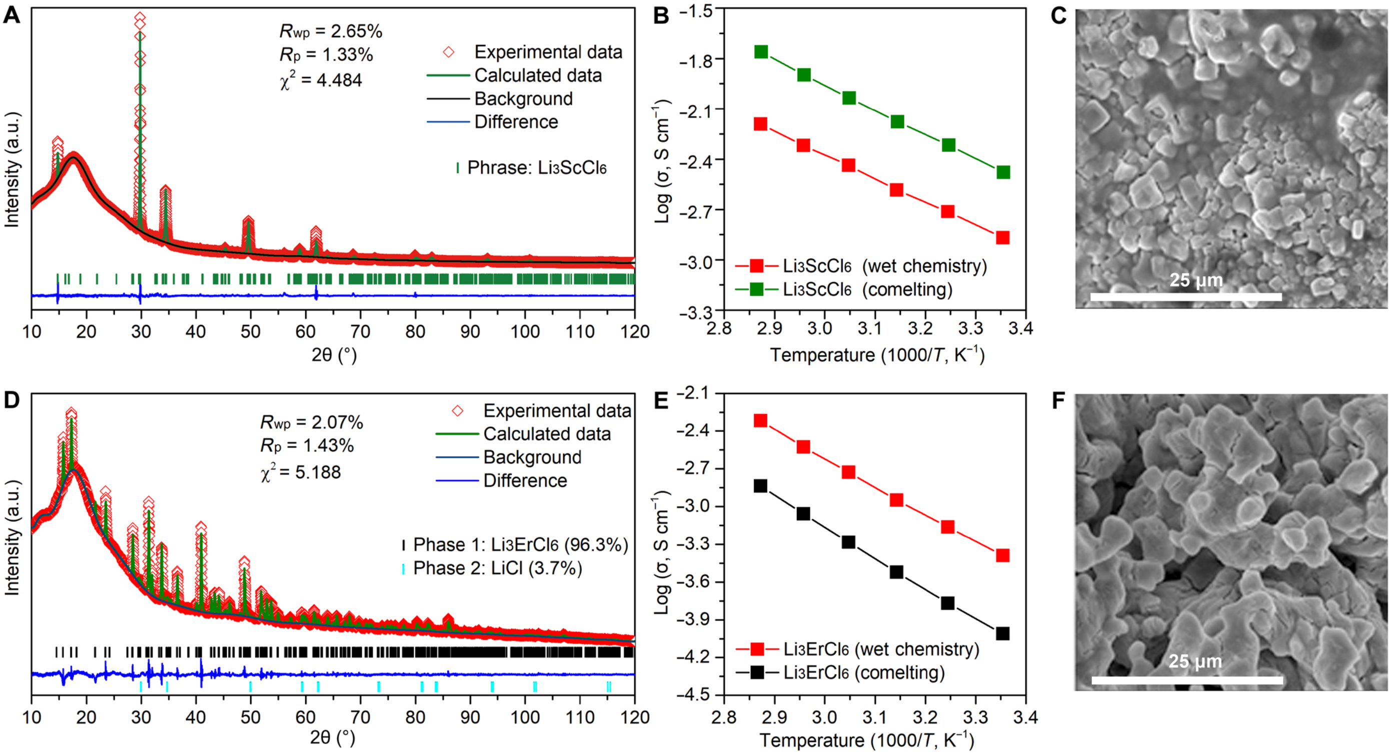

Fig. 3. Structural, electrochemical, and morphological analyses of Li_3ScCl_6 and Li_3ErCl_6 synthesized by the wet-chemistry method. (**A**) Slow-scanned XRD pattern and Rietveld refinement result of Li_3ScCl_6 synthesized by the wet-chemistry method. (**B**) Arrhenius plots of Li_3ScCl_6 synthesized by the wet-chemistry method and comelting method. (**C**) SEM image of Li_3ScCl_6 synthesized by the wet-chemistry method. (**D**) Slow-scanned XRD pattern and Rietveld refinement result of Li_3ErCl_6 prepared by the wet-chemistry method. (**E**) Arrhenius plot of Li_3ErCl_6 in comparison with comelting synthesized Li_3ErCl_6. (**F**) SEM image of wet-chemistry Li_3ErCl_6.

larger than the solid-state reaction method. Overall, it is likely that the microstrain-induced local structural change is beneficial for Li-ion transport along the *ab* plane in the halide electrolytes with a hexagonal closest packing anion framework (i.e., Li_3YCl_6 and Li_3ErCl_6), while the microstrain in halide electrolytes with a cubic closest packing sublattice (i.e., Li_3ScCl_6 and Li_3YBr_6,) might not be favorable. These findings, while preliminary, suggest that understanding the role of localized microstrain in solid electrolytes is a bright direction to further boost their ionic conductivity.

Interfacial stability toward lithium metal anodes

So far, ASSLMBs based on halide electrolytes have seldom been demonstrated because of the incompatibility between lithium metal and halide electrolytes (*36*, *37*, *41*). To address this dilemma, we adopted the most common strategy, interface modification. On the basis of our previous studies, sulfide electrolytes demonstrated excellent stability against lithium metal (*49*). Sulfide electrolytes are not thermodynamically stable against lithium metal; however, the self-limited reactions between lithium metal and Li_6PS_5Cl can generate a stable interface consisting of Li_2S, Li_3P, and LiCl, constructing a Li^+-conductive interface (fig. S13) (*50*). In addition, it was recently found that the interface resistance between sulfide electrolytes and halide electrolytes is almost negligible (*41*). Therefore, it is reasonable to construct a stable Li^+-conductive interface between halide electrolytes and lithium metal by inserting a thin layer of Li_6PS_5Cl. Figure 4A shows the EIS of $Li/Li_3YCl_6/Li$ symmetrical cells in a function of time. The semicircle at the high frequency corresponds to the Li_3YCl_6 bulk resistance. With the increase in time, another semicircle at the middle frequency appeared and enlarged, suggesting that a new interface was growing at the Li/Li_3YCl_6 interface (*41*). This phenomenon is reasonable because Li_3YCl_6 is easily reduced by lithium metal (*37*), forming Li_3Y alloys with high electronic conductivity (Fig. 4D). Therefore, Li_3YCl_6/Li interface is a mixed Li^+/e^--conductive interface, leading to a continuous reduction of Li_3YCl_6 during the Li^+ plating/stripping process. To prevent the formation of the unfavorable mixed Li^+/e^--conductive interface, a thin layer of highly Li^+-conductive Li_6PS_5Cl was inserted at the Li_3YCl_6/Li interface. Figure 4B shows the EIS profile of $Li/Li_6PS_5Cl/Li_3YCl_6/Li_6PS_5Cl/Li$ symmetric cells. Comparatively, the semicircle at the middle frequency was absent, suggesting that the interfacial reactions between halide electrolytes and lithium metal were successfully suppressed. However, the overall impedance still increased with time, suggesting that interfacial reactions between Li_6PS_5Cl and lithium metal occurred. Considering the narrow electrochemical windows of Li_6PS_5Cl, Li_6PS_5Cl reacts with lithium metal spontaneously even without electrochemical process, generating Li_2S, Li_3P, and LiCl. Li_3P is highly Li^+ conductive, while Li_2S and LiCl are electronically insulative (Fig. 4E). Therefore, the formed interface between Li_6PS_5Cl and lithium metal is an excellent Li^+-conductive interface that is highly preferable in ASSLMBs. Figure 4C compares the Li^+ plating/stripping behaviors of $Li/Li_3YCl_6/Li$ and $Li/Li_6PS_5Cl/Li_3YCl_6/Li_6PS_5Cl/Li$ symmetrical cells over 500 hours. The overpotential of $Li/Li_3YCl_6/Li$ gradually increased to about 600 mV. As a sharp contrast, the $Li/Li_6PS_5Cl/Li_3YCl_6/Li_6PS_5Cl/Li$ can be stably cycled for up to 500 hours with a small overpotential of less than 100 mV.

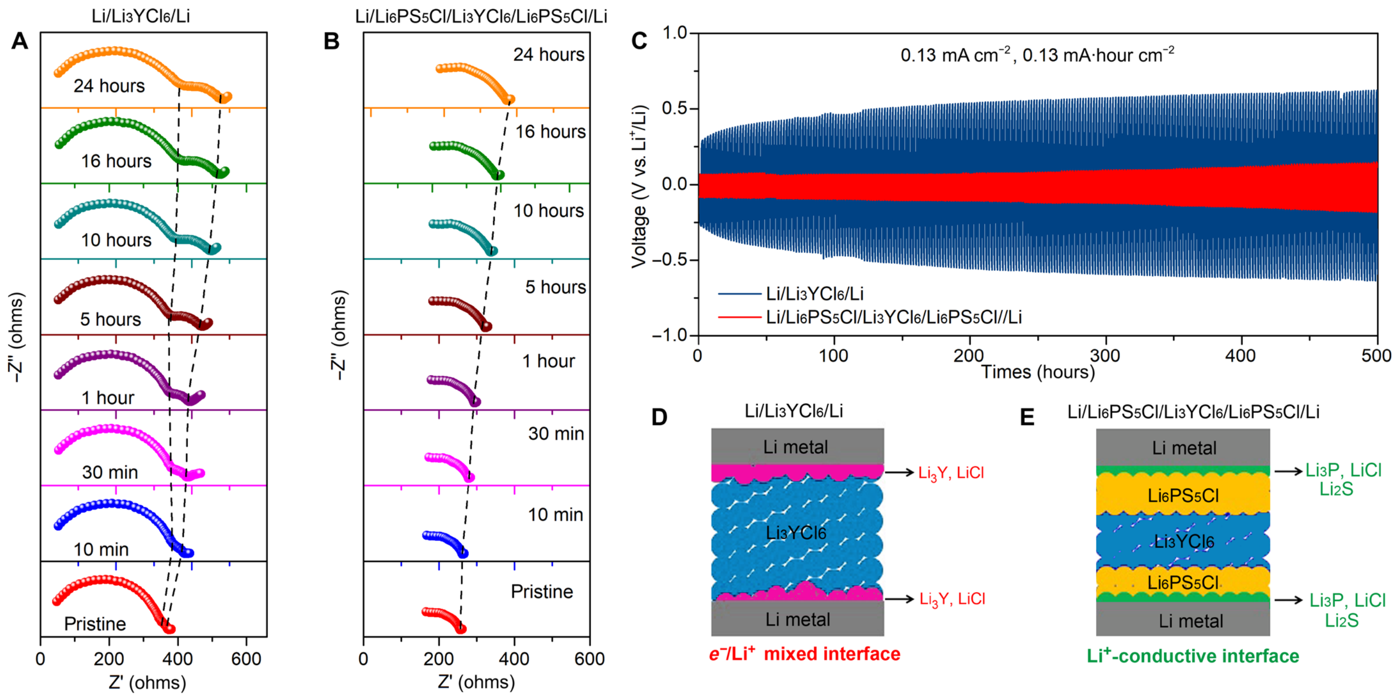

Fig. 4. Interfacial stability between halide electrolytes and lithium metal anodes. (**A**) Time-resolved EIS spectra of Li/Li_3YCl_6/Li symmetric cells. (**B**) Time-resolved EIS spectra of Li/Li_6PS_5Cl/Li_3YCl_6/Li_6PS_5Cl/Li symmetric cells. (**C**) The symmetric cell performance comparison. (**D**) The mixed electronic and ionic interface between lithium metal and Li_3YCl_6. (**E**) The Li^+-conductive interface between Li_3YCl_6 and Li enabled by a thin layer of Li_6PS_5Cl.

Furthermore, x-ray photoelectron spectroscopy (XPS) was performed to analyze the Li_3YCl_6/Li interface and Li_3YCl_6/Li_6PS_5Cl/Li interface after cycling (fig. S14). As confirmed by XPS analysis, Li_3YCl_6 was reduced or decomposed by lithium metal after 100 hours of cycling, which is the reason for the increasing overpotential observed during the platting/stripping process. As a sharp comparison, the interface is changed into a solely ionic conductive interface consisting of Li_2S, LiCl, and Li_3P, which effectively blocks electrons across the interface, thus well stabilizing the anode interface for ASSLMBs.

ASSLMBs based on bilayer solid electrolytes

As a stable interface between halide electrolytes and lithium metal was successfully constructed, an ASSLMB based on halide electrolyte can be fabricated. Figure 5A illustrates the configuration of ASSLMBs based on Li_3YCl_6, in which a thin layer of Li_6PS_5Cl is inserted between Li_3YCl_6 and lithium metal anode to form a stable anode interface. It should be mentioned that $LiCoO_2$ (LCO) is used without any interfacial coating because of the high oxidative stability of Li_3YCl_6 (>4.25 V versus Li^+/Li). Figure 5B shows the initial charge/discharge curves of the ASSLMBs at 0.1 C. The discharge capacity was 139.1 mA·hour g^{-1}, and the initial coulombic efficiency (CE) was as high as 98.1%. The high discharge capacity is due to the intimate solid-solid contact between Li_3YCl_6 and LCO (figs. S15 to S17). The high CE is ascribed to the use of lithium metal as the anode, which could supply any deficient Li ions unlike pure indium (In) foil or Li-In alloys. Figure 5C shows the cycling stability of ASSLMBs. It maintained a capacity of 118.5 mA·hour g^{-1} with a high CE of ~99.3% on average over 50 cycles. Figure 5D exhibits the rate performance of ASSLMBs. Because of the limited ionic conductivity of Li_3YCl_6, the RT rate performance was limited, but much better rate performance can be demonstrated at an elevated testing temperature of 60°C. A discharge capacity of 58.6 mA·hour g^{-1} was delivered at a current rate of 1 C, indicating that not only the solid-solid contact but also the high ionic conductivity of solid electrolytes is crucial for the rate performance of ASSLMBs. To verify this assumption, we further tested the rate performance of Li_3ScCl_6-based ASSLMBs (Fig. 5E), in which single-crystal $LiNi_{0.6}Mn_{0.2}Co_{0.2}O_2$ (SC-NMC622) was chosen as the active material because of its advantages in mechanical integrity and ion dynamics (*51*). Because of the high ionic conductivity of Li_3ScCl_6 (1.25 mS cm^{-1}), ASSLMBs with a configuration of SC-NMC622|Li_3ScCl_6|Li_6PS_5Cl|Li showed a high initial capacity of 166.9 mA·hour g^{-1} with a CE of 85.6%. The ASSLMB retained a capacity of 81.1 mA·hour g^{-1} at 1 C and 38.6 mA·hour g^{-1} at 2 C at RT. The capacity remained at 85.9 mA·hour g^{-1} at 0.2 C after 100 cycles. The energy density of ASSLMBs demonstrated in this work outperforms previous results, as compared in table S9.

DISCUSSION

In summary, ammonium-assisted wet chemistry is reported to be a universal strategy to synthesize various solid-state halide electrolytes with a submicrometer size. The obtained halide electrolytes can exhibit decent RT ionic conductivity (up to 1.25 mS cm^{-1}). Moreover, a thin layer of sulfide electrolyte was proven to be effective in preventing anode interfacial reactions between halide electrolytes and lithium metal. As a result, halide-based ASSLMBs with excellent electrochemical performance have been successfully demonstrated. This work provides an exemplary platform for developing halide-based ASSLMBs with high energy density. We believe that this universal ammonium-assisted wet chemistry can be further explored to synthesize other

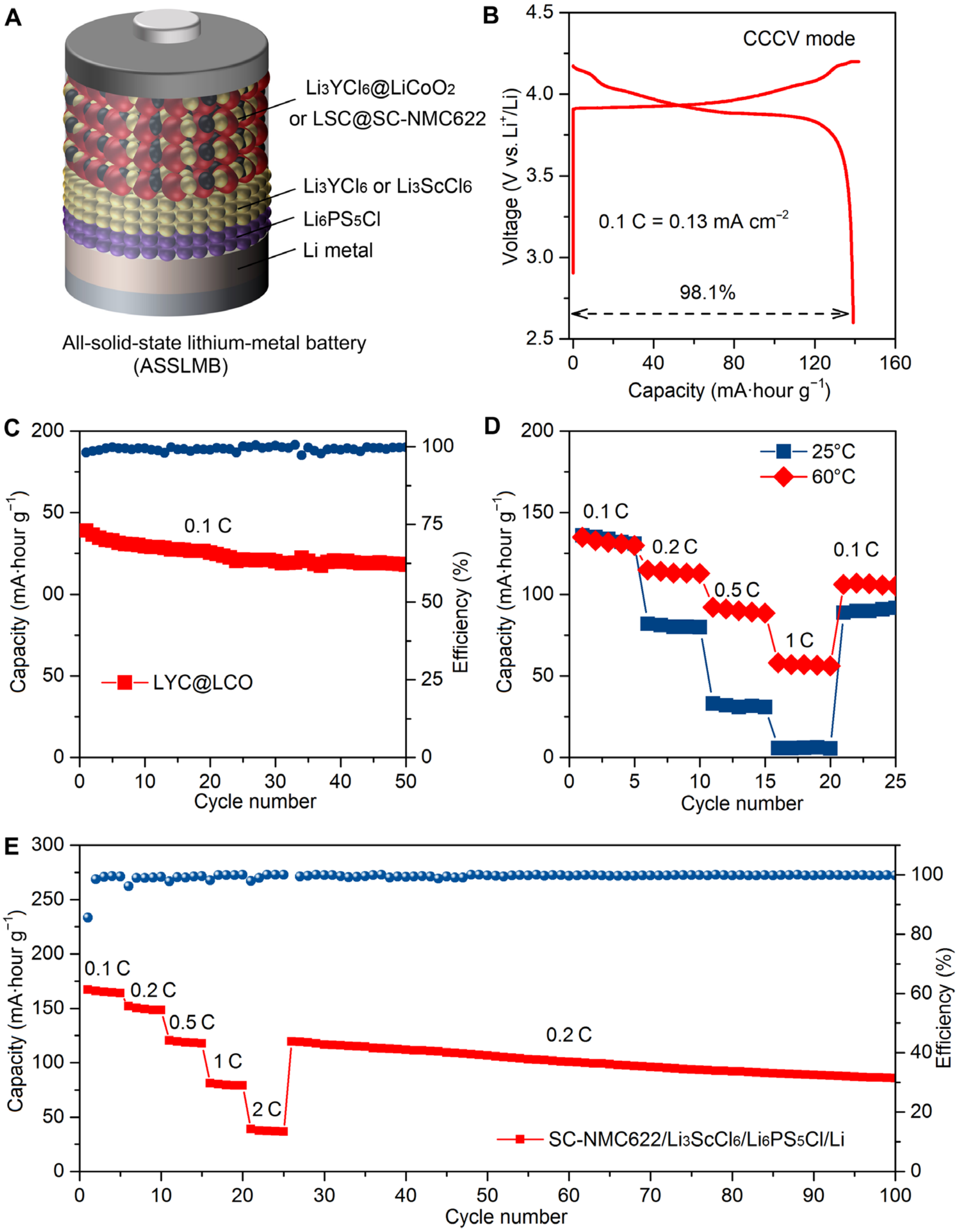

Fig. 5. Electrochemical performance of ASSLMBs based on halide electrolytes. (**A**) Schematic diagram of ASSLMBs. (**B**) Initial charge/discharge curves of ASSLMBs under 0.1 C at RT (2.6 to 4.2 V versus Li$^+$/Li). (**C**) Cycling stability of ASSLMBs. (**D**) Rate performance under RT and 60°C. (**E**) Rate performance of ASSLMBs with a configuration of SC-NMC622|Li_3ScCl_6|Li_6PS_5Cl|Li at RT (2.8 to 4.4 V versus Li$^+$/Li). CCCV, constant current constant voltage; LYC, Li_3YCl_6; LSC, Li_3ScCl_6.

solid-state electrolytes with a general formula of A_3MX_6 (A = Li and Na; M = trivalent metals; X = Cl, Br, and I).

MATERIALS AND METHODS

Ammonium-assisted synthesis of Li_3MX_6 (M = Y, Sc, and Er; X = Cl and Br)

First, stoichiometric mixtures of LiCl (99.9%; Sigma-Aldrich), NH_4Cl (>99.5%; Sigma-Aldrich), and $YCl_3·6H_2O$ (99.99%; Sigma-Aldrich) were weighed and dissolved into water. After complete dissolution, the mixture solution was transferred to a glass oven (Büchi glass oven, B-585) for drying at 80°C under vacuum. After drying, the white powder was transferred to a glove box and pressed into pellets for annealing at various temperatures (350° to 550°C) for 5 hours, respectively. The heating rate was 2°C min^{-1}. Similar procedures were followed to synthesize Li_3YBr_6, Li_3ScCl_6, and Li_3ErCl_6 but changing the $YCl_3·6H_2O$ to YBr_3 (99.9%; Sigma-Aldrich), $ScCl_3$ (99.99%; Sigma-Aldrich), and $ErCl_3$ (99.99%; Sigma-Aldrich), respectively.

Characterizations

The XRD patterns were obtained over the range of 10° to 120° (2θ) using Cu Kα x-ray radiation with λ = 1.54178 Å (Bruker AXS D8 Advance). As-prepared halide electrolytes were sealed in an air-tight holder to avoid air exposure to protect them from ambient air. The data for the XRD Rietveld refinement were collected by scanning 5 s per step with one step of 0.02°. Neutron diffraction data were collected at the NOMAD (Nanoscale-Ordered Materials Diffractometer) beamline at the Spallation Neutron Source, Oak Ridge National Laboratory. The Rietveld refinement was performed using GSAS-II (*52*). The crystal structure was visualized using VESTA (*53*). SEM images were recorded using a Hitachi S-4800 field emission SEM equipped with energy-dispersive spectroscopy. The XPS data were collected with a monochromatic Al Kα source (1486.6 eV) using the Thermo Scientific K-Alpha Spectrometer at the University of Toronto.

Electrochemical characterizations

Ionic conductivities of as-prepared halide electrolytes Li_3MCl_6 (M = Er, Y, and Sc) with a configuration of carbon|Li_3MCl_6|carbon were measured by the AC impedance technique on a VMP3 potentiostat/galvanostat (BioLogic). The halide electrolyte pellet was isostatically pressed under 500 MPa. Impedance was measured at a frequency range of 7 MHz to 0.1 Hz using an SP-300 impedance analyzer (BioLogic). The electrochemical stability was evaluated by cyclic voltammetry measurements using versatile multichannel potentiostat 3/Z (VMP3) with a Li/Li_3YCl_6/Li_3YCl_6-AB cell in a scan range of 0 to 5 V (versus Li^+/Li) at 0.1 mV s^{-1}. To evaluate cycling performance, ASSLMBs with a configuration of cathode|halide electrolyte|Li_6PS_5Cl|Li metal are fabricated. First, 70-mg halide electrolytes (Li_3YCl_6 or Li_3ScCl_6) and 30-mg Li_6PS_5Cl were pressed at 100 MPa. Second, 12-mg cathode composites (active materials:halide electrolyte = 85%:15%) were spread on one side of halide electrolyte pellets and pressed at 500 MPa. Third, a Li foil was attached to another side of halide electrolyte pellets and pressed at 50 MPa. Last, the mold cells were added with some pressure by a torque wrench (60 N·m). The LCO|Li_3YCl_6|Li_6PS_5Cl|Li battery was charged to 4.2 V at 0.1 C and then charged to 0.01 C with a constant voltage of 4.2 V. The SC-NMC622|Li_3ScCl_6|Li_6PS_5Cl|Li battery was charged to 4.4 V at 0.1 C and then discharged to 2.8 V (versus Li^+/Li). The cathode composite mass is 12 mg. The electrochemical performance was evaluated using the Neware system.

SUPPLEMENTARY MATERIALS

Supplementary material for this article is available at https://science.org/doi/10.1126/sciadv.abh1896

REFERENCES AND NOTES

1. Z. Gao, H. Sun, L. Fu, F. Ye, Y. Zhang, W. Luo, Y. Huang, Promises, challenges, and recent progress of inorganic solid-state electrolytes for all-solid-state lithium batteries. *Adv. Mater.* **30**, 1705702 (2018).
2. A. Manthiram, X. Yu, S. Wang, Lithium battery chemistries enabled by solid-state electrolytes. *Nat. Rev. Mater.* **2**, 16103 (2017).
3. L. Liu, J. Xu, S. Wang, F. Wu, H. Li, L. Chen, Practical evaluation of energy densities for sulfide solid-state batteries. *eTransportation* **1**, 100010 (2019).
4. B. Wu, S. Wang, W. J. Evans Iv, D. Z. Deng, J. Yang, J. Xiao, Interfacial behaviours between lithium ion conductors and electrode materials in various battery systems. *J. Mater. Chem. A* **4**, 15266–15280 (2016).
5. D. Zhou, D. Shanmukaraj, A. Tkacheva, M. Armand, G. Wang, Polymer electrolytes for lithium-based batteries: Advances and prospects. *Chem* **5**, 2326–2352 (2019).
6. H. Zhang, C. Li, M. Piszcz, E. Coya, T. Rojo, L. M. Rodriguez-Martinez, M. Armand, Z. Zhou, Single lithium-ion conducting solid polymer electrolytes: Advances and perspectives. *Chem. Soc. Rev.* **46**, 797–815 (2017).
7. L. Yue, J. Ma, J. Zhang, J. Zhao, S. Dong, Z. Liu, G. Cui, L. Chen, All solid-state polymer electrolytes for high-performance lithium ion batteries. *Energy Storage Mater.* **5**, 139–164 (2016).
8. V. Thangadurai, S. Narayanan, D. Pinzaru, Garnet-type solid-state fast Li ion conductors for Li batteries: Critical review. *Chem. Soc. Rev.* **43**, 4714–4727 (2014).
9. M. Jia, N. Zhao, H. Huo, X. Guo, Comprehensive investigation into garnet electrolytes toward application-oriented solid lithium batteries. *Electrochem. Energy Rev.* **3**, 656–689 (2020).
10. Q. Zhang, D. Cao, Y. Ma, A. Natan, P. Aurora, H. Zhu, Sulfide-based solid-state electrolytes: Synthesis, stability, and potential for all-solid-state batteries. *Adv. Mater.* **31**, 1901131 (2019).
11. S. Kim, H. Oguchi, N. Toyama, T. Sato, S. Takagi, T. Otomo, D. Arunkumar, N. Kuwata, J. Kawamura, S.-i. Orimo, A complex hydride lithium superionic conductor for high-energy-density all-solid-state lithium metal batteries. *Nat. Commun.* **10**, 1081 (2019).
12. H. Maekawa, M. Matsuo, H. Takamura, M. Ando, Y. Noda, T. Karahashi, S.-i. Orimo, Halide-stabilized $LiBH_4$, a room-temperature lithium fast-ion conductor. *J. Am. Chem. Soc.* **131**, 894–895 (2009).
13. M. Matsuo, S.-i. Orimo, Lithium fast-ionic conduction in complex hydrides: Review and prospects. *Adv. Energy Mater.* **1**, 161–172 (2011).
14. Y. Yan, R.-S. Kühnel, A. Remhof, L. Duchêne, E. C. Reyes, D. Rentsch, Z. Łodziana, C. Battaglia, A lithium amide-borohydride solid-state electrolyte with lithium-ion conductivities comparable to liquid electrolytes. *Adv. Energy Mater.* **7**, 1700294 (2017).
15. W. S. Tang, M. Matsuo, H. Wu, V. Stavila, W. Zhou, A. A. Talin, A. V. Soloninin, R. V. Skoryunov, O. A. Babanova, A. V. Skripov, A. Unemoto, S.-I. Orimo, T. J. Udovic, Liquid-like ionic conduction in solid lithium and sodium monocarba-closo-decaborates near or at room temperature. *Adv. Energy Mater.* **6**, 1502237 (2016).
16. X. Li, J. Liang, X. Yang, K. R. Adair, C. Wang, F. Zhao, X. Sun, Progress and perspectives on halide lithium conductors for all-solid-state lithium batteries. *Energy Environ. Sci.* **13**, 1429–1461 (2020).
17. J. Liang, X. Li, K. R. Adair, X. Sun, Metal halide superionic conductors for all-solid-state batteries. *Acc. Chem. Res.* **54**, 1023–1033 (2021).
18. J. Wu, S. Liu, F. Han, X. Yao, C. Wang, Lithium/sulfide all-solid-state batteries using sulfide electrolytes. *Adv. Mater.* **33**, 2000751 (2021).
19. T. Asano, A. Sakai, S. Ouchi, M. Sakaida, A. Miyazaki, S. Hasegawa, Solid halide electrolytes with high lithium-ion conductivity for application in 4 V class bulk-type all-solid-state batteries. *Adv. Mater.* **38**, 1803075 (2018).
20. X. Li, J. Liang, N. Chen, J. Luo, K. R. Adair, C. Wang, M. N. Banis, T. K. Sham, L. Zhang, S. Zhao, S. Lu, H. Huang, R. Li, X. Sun, Water-mediated synthesis of a superionic halide solid electrolyte. *Angew. Chem. Int. Ed.* **131**, 16579–16584 (2019).
21. C. Zhao, J. Liang, X. Li, N. Holmes, C. Wang, J. Wang, F. Zhao, S. Li, Q. Sun, X. Yang, J. Liang, X. Lin, W. Li, R. Li, S. Zhao, H. Huang, L. Zhang, S. Lu, X. Sun, Halide-based solid-state electrolyte as an interfacial modifier for high performance solid-state Li–O_2 batteries. *Nano Energy* **75**, 105036 (2020).
22. C. Wang, J. Liang, M. Jiang, X. Li, S. Mukherjee, K. Adair, M. Zheng, Y. Zhao, F. Zhao, S. Zhang, R. Li, H. Huang, S. Zhao, L. Zhang, S. Lu, C. V. Singh, X. Sun, Interface-assisted in-situ growth of halide electrolytes eliminating interfacial challenges of all-inorganic solid-state batteries. *Nano Energy* **76**, 105015 (2020).
23. X. Li, J. Liang, J. Luo, M. Norouzi Banis, C. Wang, W. Li, S. Deng, C. Yu, F. Zhao, Y. Hu, T.-K. Sham, L. Zhang, S. Zhao, S. Lu, H. Huang, R. Li, K. R. Adair, X. Sun, Air-stable Li_3InCl_6 electrolyte with high voltage compatibility for all-solid-state batteries. *Energy Environ. Sci.* **12**, 2665–2671 (2019).
24. J. Liang, X. Li, S. Wang, K. R. Adair, W. Li, Y. Zhao, C. Wang, Y. Hu, L. Zhang, S. Zhao, S. Lu, H. Huang, R. Li, Y. Mo, X. Sun, Site-occupation-tuned superionic Li_xScCl_{3+x} halide solid electrolytes for all-solid-state batteries. *J. Am. Chem. Soc.* **142**, 7012–7022 (2020).
25. X. Li, J. Liang, K. R. Adair, J. Li, W. Li, F. Zhao, Y. Hu, T.-K. Sham, L. Zhang, S. Zhao, S. Lu, H. Huang, R. Li, N. Chen, X. Sun, Origin of superionic $Li_3Y_{1-x}In_xCl_6$ halide solid electrolytes with high humidity tolerance. *Nano Lett.* **20**, 4384–4392 (2020).
26. C. Yu, Y. Li, K. R. Adair, W. Li, K. Goubitz, Y. Zhao, M. J. Willans, M. A. Thijs, C. Wang, F. Zhao, Q. Sun, S. Deng, J. Liang, X. Li, R. Li, T.-K. Sham, H. Huang, S. Lu, S. Zhao, L. Zhang, L. van Eijck, Y. Huang, X. Sun, Tuning ionic conductivity and electrode compatibility of Li_3YBr_6 for high-performance all solid-state Li batteries. *Nano Energy* **77**, 105097 (2020).
27. K.-H. Park, K. Kaup, A. Assoud, Q. Zhang, X. Wu, L. F. Nazar, High-voltage superionic halide solid electrolytes for all-solid-state Li-ion batteries. *ACS Energy Lett.* **5**, 533–539 (2020).
28. L. Zhou, C. Y. Kwok, A. Shyamsunder, Q. Zhang, X. Wu, L. F. Nazar, A new halospinel superionic conductor for high-voltage all solid state lithium batteries. *Energy Environ. Sci.* **13**, 2056–2063 (2020).
29. R. Schlem, S. Muy, N. Prinz, A. Banik, Y. Shao-Horn, M. Zobel, W. G. Zeier, Mechanochemical synthesis: A tool to tune cation site disorder and ionic transport properties of Li_3MCl_6(M = Y, Er) superionic conductors. *Adv. Energy Mater.* **10**, 1903719 (2020).
30. S. Muy, J. Voss, R. Schlem, R. Koerver, S. J. Sedlmaier, F. Maglia, P. Lamp, W. G. Zeier, Y. Shao-Horn, High-throughput screening of solid-state Li-ion conductors using lattice-dynamics descriptors. *iScience* **16**, 270–282 (2019).
31. R. Schlem, A. Banik, M. Eckardt, M. Zobel, W. G. Zeier, $Na_{3-x}Er_{1-x}Zr_xCl_6$—A halide-based fast sodium-ion conductor with vacancy-driven ionic transport. *ACS Appl. Energy Mater.* **3**, 10164–10173 (2020).
32. R. Schlem, T. Bernges, C. Li, M. A. Kraft, N. Minafra, W. G. Zeier, Lattice dynamical approach for finding the lithium superionic conductor Li_3ErI_6. *ACS Appl. Energy Mater.* **3**, 3684–3691 (2020).

33. H. Kwak, D. Han, J. Lyoo, J. Park, S. H. Jung, Y. Han, G. Kwon, H. Kim, S.-T. Hong, K.-W. Nam, Y. S. Jung, New cost-effective halide solid electrolytes for all-solid-state batteries: Mechanochemically prepared Fe^{3+}-substituted Li_2ZrCl_6. *Adv. Energy Mater.* **11**, 2003190 (2021).
34. M. Feinauer, H. Euchner, M. Fichtner, M. A. Reddy, Unlocking the potential of fluoride-based solid electrolytes for solid-state lithium batteries. *ACS Appl. Energy Mater.* **2**, 7196–7203 (2019).
35. J. Xie, A. D. Sendek, E. D. Cubuk, X. Zhang, Z. Lu, Y. Gong, T. Wu, F. Shi, W. Liu, E. J. Reed, Y. Cui, Atomic layer deposition of stable $LiAlF_4$ lithium ion conductive interfacial layer for stable cathode cycling. *ACS Nano* **11**, 7019–7027 (2017).
36. D. Park, H. Park, Y. Lee, S.-O. Kim, H.-G. Jung, K. Y. Chung, J. H. Shim, S. Yu, Theoretical design of lithium chloride superionic conductors for all-solid-state high-voltage lithium-ion batteries. *ACS Appl. Mater. Interfaces* **12**, 34806–34814 (2020).
37. S. Wang, Q. Bai, A. M. Nolan, Y. Liu, S. Gong, Q. Sun, Y. Mo, Lithium chlorides and bromides as promising solid-state chemistries for fast ion conductors with good electrochemical stability. *Angew. Chem. Int. Ed.* **58**, 8039–8043 (2019).
38. Z. Xu, X. Chen, K. Liu, R. Chen, X. Zeng, H. Zhu, Influence of anion charge on Li ion diffusion in a new solid-state electrolyte, Li3LaI6. *Chem. Mater.* **31**, 7425–7433 (2019).
39. Y. Liu, S. Wang, A. M. Nolan, C. Ling, Y. Mo, Tailoring the cation lattice for chloride lithium-ion conductors. *Adv. Energy Mater.* **10**, 2002356 (2020).
40. A. Miura, N. C. Rosero-Navarro, A. Sakuda, K. Tadanaga, N. H. H. Phuc, A. Matsuda, N. Machida, A. Hayashi, M. Tatsumisago, Liquid-phase syntheses of sulfide electrolytes for all-solid-state lithium battery. *Nat. Rev. Chem.* **3**, 189–198 (2019).
41. L. Riegger, R. Schlem, J. Sann, W. G. Zeier, J. Janek, Lithium-metal anode instability of the superionic halide solid electrolytes and the implications for solid-state batteries. *Angew. Chem. Int. Ed.* **60**, 6718–6723 (2021).
42. G. Meyer, E. Garcia, J. D. Corbett, The ammonium chloride route to anhydrous rare earth chlorides—The example of YCl_3, in *Inorganic Syntheses* (Inorganic Syntheses Inc., 1989), vol. 25, pp. 146–150.
43. M. Simon, G. Meyer, The oxidation of tantalum with ammonium chloride as an example of a novel route to early transitional metal–nitrogen cluster compounds. Synthesis and crystal structure of $(NH_4)_6[Ta_5(NH)_4Cl_{17}]$. *J. Chem. Soc. Chem. Commun.* **5**, 460–461 (1993).
44. A. Bohnsack, F. Stenzel, A. Zajonc, G. Balzer, M. S. Wickleder, G. Meyer, Ternary halides of the A_3MX_6 type. VI. Ternäry chlorides of the rare-earth elements with lithium, Li_3MCl_6 (M = Tb-Lu, Y, Sc): Synthesis, crystal structures, and ionic motion. *Z. Anorg. Allg. Chem.* **623**, 1067–1073 (1997).
45. F. Han, A. S. Westover, J. Yue, X. Fan, F. Wang, M. Chi, D. N. Leonard, N. J. Dudney, H. Wang, C. Wang, High electronic conductivity as the origin of lithium dendrite formation within solid electrolytes. *Nat. Energy* **4**, 187–196 (2019).
46. R. Schlem, A. Banik, S. Ohno, E. Suard, W. G. Zeier, Insights into the lithium sub-structure of superionic conductors Li_3YCl_6 and Li_3YBr_6. *Chem. Mater.* **33**, 327–337 (2021).
47. H. Ito, K. Shitara, Y. Wang, K. Fujii, M. Yashima, Y. Goto, C. Moriyoshi, N. C. Rosero-Navarro, A. Miura, K. Tadanaga, Kinetically stabilized cation arrangement in Li_3YCl_6 superionic conductor during solid-state reaction. *Adv. Sci.* **2021**, 2101413 (2021).
48. E.-J. Lee, Z. Chen, H.-J. Noh, S. C. Nam, S. Kang, D. H. Kim, K. Amine, Y.-K. Sun, Development of microstrain in aged lithium transition metal oxides. *Nano Lett.* **14**, 4873–4880 (2014).
49. C. Yu, Y. Li, M. Willans, Y. Zhao, K. R. Adair, F. Zhao, W. Li, S. Deng, J. Liang, M. N. Banis, R. Li, H. Huang, L. Zhang, R. Yang, S. Lu, Y. Huang, X. Sun, Superionic conductivity in lithium argyrodite solid-state electrolyte by controlled Cl-doping. *Nano Energy* **69**, 104396 (2020).
50. J. M. Doux, H. Nguyen, D. H. Tan, A. Banerjee, X. Wang, E. A. Wu, C. Jo, H. Yang, Y. S. Meng, Stack pressure considerations for room-temperature all-solid-state lithium metal batteries. *Adv. Energy Mater.* **10**, 1903253 (2020).
51. C. Wang, R. Yu, S. Hwang, J. Liang, X. Li, C. Zhao, Y. Sun, J. Wang, N. Holmes, R. Li, H. Huang, S. Zhao, L. Zhang, S. Lu, D. Su, X. Sun, Single crystal cathodes enabling high-performance all-solid-state lithium-ion batteries. *Energy Storage Mater.* **30**, 98–103 (2020).
52. B. H. Toby, R. B. Von Dreele, GSAS-II: The genesis of a modern open-source all purpose crystallography software package. *J. Appl. Crystallogr.* **46**, 544–549 (2013).
53. K. Momma, F. Izumi, *VESTA 3* for three-dimensional visualization of crystal, volumetric and morphology data. *J. Appl. Crystallogr.* **44**, 1272–1276 (2011).

Acknowledgments: C.W. thanks Mitacs Accelerate Fellowships for their support. We thank S. Wang and Y. Mo from the University of Maryland for constructive discussion and suggestions. **Funding:** This work was supported by the Natural Sciences and Engineering Research Council of Canada (NSERC), Canada Research Chair Program (CRC), Canada Foundation for Innovation (CFI), Ontario Research Fund (ORF), China Automotive Battery Research Institute Co. Ltd., Glabat Solid-State Battery Inc., and University of Western Ontario. Neutron diffraction analysis conducted at the NOMAD beamlines at ORNL's Spallation Neutron Source was sponsored by the Scientific User Facilities Division, Office of Basic Sciences, U.S. Department of Energy. **Author contributions:** J.W. and J.Li. conceived the study. X.S. and J.W. supervised the project. C.W. planned and performed the experiments, and collected and analyzed the data. J.Li., J.Lu., J. Liu, X.L., F.Z., S.Z., and L.Z. assisted with the experiments and characterizations. C.W. wrote the manuscript. J.Lu. polished the language. All authors discussed the results and commented on the manuscript. **Competing interests:** The authors declare that they have no financial and other competing interests. **Data and materials availability:** All data needed to evaluate the conclusions in the paper are present in the paper and/or the Supplementary Materials. Additional data related to this paper may be requested from the authors.

Submitted 22 February 2021
Accepted 19 July 2021
Published 8 September 2021
10.1126/sciadv.abh1896

Citation: C. Wang, J. Liang, J. Luo, J. Liu, X. Li, F. Zhao, R. Li, H. Huang, S. Zhao, L. Zhang, J. Wang, X. Sun, A universal wet-chemistry synthesis of solid-state halide electrolytes for all-solid-state lithium-metal batteries. *Sci. Adv.* **7**, eabh1896 (2021).